

# Persistence of post-Newtonian structure in binary black hole mergers

Viviana A. Cáceres-Barbosa

*Institute for Gravitation and the Cosmos, Department of Physics,  
The Pennsylvania State University, University Park, PA 16802, USA \**

(Dated: September 1, 2025)

We analyze the spherical harmonic mode amplitudes of quasi-circular, nonprecessing binary black hole mergers using 283 numerical relativity (NR) simulations from the SXS, RIT, and MAYA catalogs. We construct fits using the leading-order post-Newtonian (PN) dependence on intrinsic parameters, replacing the PN velocity with fit coefficients. We compare these to polynomial fits in symmetric mass ratio and spin. We analyze  $(\ell, m)$  modes with  $\ell \leq 4$  from late inspiral ( $t = -500M$  relative to the  $(2, 2)$  peak) to post-merger ( $t = 40M$ ). For nonspinning systems, the  $(2, 2)$ ,  $(2, 1)$ , and  $(3, 3)$  modes retain the leading-order PN dependence on mass ratio throughout the merger. Higher-order modes deviate from the PN dependence only near and after the merger, where polynomial fits of degree  $N \leq 3$  can capture the amplitude behavior up to  $40M$ . For aligned-spin systems at fixed mass ratio, the  $(2, 1)$  mode retains its PN spin dependence, while the  $(3, 2)$  and  $(4, 3)$  modes exhibit a quadratic spin dependence near merger. The PN-inspired fits lose accuracy with increasing mass ratio, particularly near merger. Results broadly agree across catalogs, though discrepancies appear in the  $(3, 1)$ ,  $(4, 2)$ , and  $(4, 1)$  modes, likely from resolution differences. Our results clarify the extent to which PN structure persists in mode amplitudes and show that simple polynomial models can capture strong-field behavior near merger, enabling efficient and interpretable waveform modeling in this regime.

## I. INTRODUCTION

Recent advances in gravitational wave (GW) detections [1] have dramatically improved our ability to observe binary black hole (BBH) mergers, opening opportunities to study their dynamics, test general relativity, and describe the population of black hole binaries. The essential tool for these analyses is the *waveform*, which describes the time evolution of the strain that arrives at gravitational-wave detectors, such as LIGO<sup>1</sup> [2], Virgo [3], and KAGRA<sup>2</sup> [4].

The waveform of a BBH system in a quasi-circular orbit is characterized by eight intrinsic parameters: the two black-hole masses and the six spin components. Efficiently extracting these parameters from an observed gravitational waveform and, conversely, constructing accurate waveforms for different intrinsic parameters helps maximize the scientific return of GW observations.

The most precise method for constructing gravitational waveforms is by numerically solving Einstein's field equations [5]. However, numerical relativity (NR) is computationally expensive and can only provide solutions for discrete points in the intrinsic parameter space. To overcome this limitation, approximation methods are necessary.

During the early inspiral phase, when the two compact objects are widely separated and moving slowly, the post-Newtonian (PN) approximation provides an effective description of the waveform [6]. However, as the binary approaches the merger, the PN expansion breaks

down due to the onset of strong-field effects and nonlinearities. In this regime, NR is required to accurately model the dynamics and GW emission.

Spherical harmonics with spin-weight  $-2$  provide a basis for describing GW radiation of inspiraling BBHs at large distances from the source. Consequently, both PN and NR waveforms for binary signals are conventionally decomposed into modes using this basis [6]. Searches and Bayesian inference of signal parameters can then selectively retain modes, balancing desired precision with computational cost.

In the ringdown phase, the GW signal can be approximated by a perturbed Kerr solution as a superposition of quasinormal modes [7]. The symmetries of the system during ringdown are best described by a decomposition into *spheroidal* harmonics, which correspond to the well-known quasinormal mode frequencies of a perturbed Kerr black hole. The angular indices specifying spheroidal harmonics are different from those specifying the spherical harmonics used for NR waveforms, a phenomenon known as mode-mixing [8].

In principle, the amplitudes and phases of spherical or spheroidal harmonic modes can be mapped back to the intrinsic parameters of the source. While the PN expansion provides analytical expressions for this mapping in the inspiral regime, extracting similar relationships near the merger is more challenging. Nevertheless, BBH detections dominated by these late-time regimes, like GW190521 [9] and GW231123 [10], are already part of the observational record. Understanding and modeling the structure of mode amplitudes and phases in the strong-field regime across the vast BBH parameter space will become increasingly important as more of these signals are detected.

Previous studies [11–17] have explored how mode am-

\* vac5288@psu.edu

<sup>1</sup> The Laser Interferometer Gravitational-Wave Observatory

<sup>2</sup> The Kamioka Gravitational Wave Detector

plitudes near merger and during the ringdown depend on the intrinsic parameters of the binary, both for spheroidal quasinormal modes in the ringdown and for spherical harmonic modes near merger. For instance, [12] and [13] investigated the dependence of the quasinormal mode spectrum on the masses and spins of the progenitor system. Using NR simulations from the BAM NR code [18], they obtained fitting functions that can describe the amplitudes of the dominant and loudest subdominant quasinormal modes in the ringdown phase. With a similar aim, the authors in [15, 16] used a Gaussian process regression to obtain mappings between intrinsic parameters and the ringdown quasinormal mode amplitudes for noneccentric precessing simulations from the Simulating eXtreme Spacetimes (SXS) catalog [19, 20]. Eccentric simulations were considered in [21], where the author used simulations from the Rochester Institute of Technology (RIT) catalog [22, 23] to obtain expressions for the ringdown mode amplitudes of nonspinning unequal-mass BBHs.

On the other hand, Ref. [11] used simulations from the SXS catalog to study the mode structure of spin-weighted spherical harmonics near the merger, using fits inspired by the leading-order dependence of the PN mode amplitudes on binary parameters. Surprisingly, they found that PN-inspired fits can describe mode amplitudes at fixed times near the merger, despite the breakdown of the PN approximation in this region. The relationship between PN and NR waveforms was also studied in Ref. [14] for eccentric BBH mergers using SXS, RIT, and MAYA [24, 25] simulations. The author similarly found that PN approximations remain valuable for constructing waveform models even close to the merger. However, discrepancies between the catalogs emerged as the mass ratio or eccentricity increased.

Inspired by previous studies suggesting that specific modes retain the leading-order PN dependence on intrinsic parameters close to the merger, we first investigate the stability of leading-order PN fits for spherical harmonic mode amplitudes from the late inspiral through the post-merger regime. We connect the early-time behavior of the recovered fit coefficients to the PN velocity to aid in the interpretation of the recovered values.

Second, we construct polynomial fits in mass ratio and spins to assess the role of beyond-leading-order dependencies in improving amplitude fits, particularly for modes where leading-order fits break down near merger. We aim to identify the simplest model required to capture the dominant physical dependencies for each mode.

Finally, for the first time, we use these methods to carry out a detailed comparison of NR simulations from the SXS, RIT, and MAYA NR catalogs. Cross-catalog comparisons provide a critical consistency check and help flag simulations where systematic differences may emerge.

The rest of this paper is organized as follows. Section II A provides an overview of the spherical harmonic decomposition and introduces relevant quantities and no-

tation. Section II B briefly describes the different NR catalogs used in this study and outlines the simulation selection criteria. Sections II C and II D present the validity of the PN expansion and the construction of PN-inspired fits, along with the methods used to assess their performance and stability. Section II E introduces fits with beyond-leading-order parameter dependencies. Section III A discusses the stability and evolution of the fit coefficients of the PN-inspired fits, evaluates their performance, interprets their connection to the true PN expansion at earlier times, and compares results across NR catalogs. Section III B presents the results of fits with higher-order dependencies and evaluates their improvements over the leading-order models. Finally, Section IV summarizes our findings and outlines directions for future work.

We use a geometrized system of units in which Newton's gravitational constant  $G$  and the speed of light  $c$  are  $c = G = 1$ .

## II. METHODS

### A. Decomposition of gravitational-wave strain into spherical harmonic modes

The multipolar expansion of GW radiation from BBH mergers can be expressed in a basis of  $-2$  spin-weighted spherical harmonics  $Y_{\ell m}^{-2}(\theta, \phi)$  as follows:

$$h(t; \theta, \phi) = \sum_{\ell=2}^{\infty} \sum_{m=-\ell}^{m=\ell} h_{\ell m}(t) Y_{\ell m}^{-2}(\theta, \phi), \quad (1)$$

where  $h$  is the complex gravitational-wave strain,  $h_{\ell m}$  are the wave modes,  $(\theta, \phi)$  are the angular coordinates specifying the direction of wave propagation, and  $t$  is the retarded time [26].

Each complex  $(\ell, m)$  mode can be written in polar form as

$$h_{\ell m}(t) = A_{\ell m}(t) e^{i\phi_{\ell m}(t)}, \quad (2)$$

where  $A_{\ell m}(t)$  and  $\phi_{\ell m}(t)$  are its amplitude and phase, respectively. The  $(2, 2)$  mode dominates the gravitational radiation emitted by a binary system [27, 28]. In this study, we analyze the amplitudes of different modes *relative to the  $(2, 2)$  mode*:

$$\hat{A}_{\ell m}(t) = \begin{cases} A_{\ell m}(t) & \text{if } (\ell, m) = (2, 2) \\ \frac{A_{\ell m}(t)}{A_{22}(t)} & \text{otherwise.} \end{cases}$$

The  $\hat{A}_{\ell m}(t)$  are extracted over the interval  $t \in (-500M, 40M)$ , where  $t = 0M$  corresponds to the peak amplitude of the  $(2, 2)$  mode.<sup>3</sup> Fig. 1 illustrates this in-

<sup>3</sup> The total mass  $M$  of the binary sets the characteristic timescale of the system. In natural units, where  $c = 1$  and  $G = 1$ , time can be expressed in terms of  $M$ , with  $1 M_{\odot} \approx 5 \times 10^{-6}$  s.

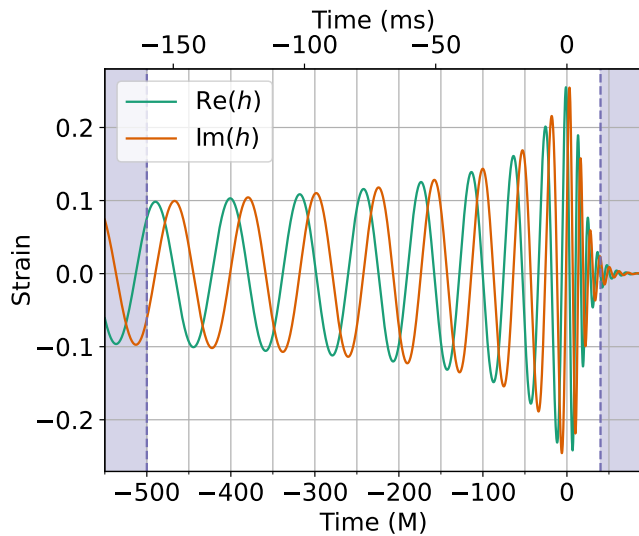


FIG. 1. Real and imaginary parts of the GW strain  $h$ , evaluated in the direction  $(\theta, \phi) = (0, 0)$  for the simulation `SXS:BBH:0305`. The total mass is set to be  $M = 65M_\odot$ . The lower horizontal axis shows time relative to the peak of the  $(2, 2)$  mode in units of  $M$ , while the upper horizontal axis converts to milliseconds. The purple shaded region marks times outside the interval  $t \in (-500M, 40M)$ , which are excluded from this work.

interval on the real and imaginary parts of the full strain  $h$  (Eq. 1) for the simulation `SXS:BBH:0305`, which appears in Fig. 1 of the GW150914 discovery paper [29]. We highlight the situation of this interval near and around the merger.

The primary dynamical parameter for a nonspinning system is its mass ratio  $q = \frac{m_1}{m_2}$ . Using the convention  $m_1 \geq m_2$ , such that  $q \geq 1$ , we can also define the symmetric mass ratio  $\eta$  and the mass asymmetry parameter  $\delta$ :

$$\eta \equiv \frac{m_1 m_2}{(m_1 + m_2)^2}, \quad (3)$$

$$\delta \equiv \frac{m_1 - m_2}{m_1 + m_2} = \sqrt{1 - 4\eta}. \quad (4)$$

In aligned-spin binaries, where the spin vectors are parallel to the orbital angular momentum, the waveform is determined by  $q$  and the spin magnitudes of the two bodies, given in dimensionless form as  $\chi_i = \frac{S_i}{m_i^2}$ , with  $i = 1, 2$  labeling the object in the binary. It is also useful to define the symmetric and antisymmetric spin combinations:

$$\chi_s \equiv \frac{1}{2} (\chi_1 + \chi_2), \quad (5)$$

$$\chi_a \equiv \frac{1}{2} (\chi_1 - \chi_2). \quad (6)$$

## B. Numerical relativity simulations

Several NR groups have performed simulations of BBH mergers using different formalisms to set initial conditions and evolve the spacetime metric [18–20, 22–25, 30]. In principle, simulations with identical initial conditions should produce the same gravitational waveform. However, differences in numerical precision, gauge choices, waveform extrapolation techniques, among other factors, can introduce discrepancies between catalogs [31].

To compare results across catalogs, we use simulations from the SXS [19, 20], RIT [22, 23], and MAYA [24, 25] catalogs. In this section, we briefly review the methods employed by each catalog and outline our simulation selection criteria.

### 1. SXS Catalog

The SXS catalog utilizes the Spectral Einstein Code [32] to perform simulations. The initial data is generated by solving the extended conformal thin-sandwich equations, which are discretized on a grid and solved using a spectral elliptic solver. Iterative tuning is applied to achieve the desired BBH properties, and the initial data is evolved for several orbits to reduce eccentricity and produce quasi-circular orbits [20].

The evolution of the initial data is carried out using a first-order version of the generalized harmonic formulation [33–35] of Einstein’s equations, with constraint damping. A multi-domain spectral method is applied, where the computational domain is partitioned into subdomains. The size, shape, and number of these subdomains are dynamically adjusted throughout the simulation using a spectral adaptive mesh refinement procedure. This refinement process relies on a specified tolerance parameter to determine whether to add or remove grid points within a subdomain or to split subdomains entirely. Most simulations are performed at multiple tolerance levels, or resolutions.

In this work, we use the highest available resolution level for each SXS simulation. The waveforms were read using the `sxs` Python package [36, 37].

### 2. RIT Catalog

The simulations in the RIT catalog are generated using the LAZEV code [38]. The initial data for RIT simulations is derived from the Bowen-York solution and computed using a generalized version of the TWO PUNCTURES code [39], which solves a coupled system of the Hamiltonian and momentum constraints. RIT simulations use PN approximations [40] to produce quasi-circular orbits.

The LAZEV code implements the Baumgarte-Shapiro-Shibata-Nakamura-Oohara-Kojima [41–43] formulation of Einstein’s equations. The code utilizes the CACTUS [44] infrastructure from the EINSTEINTOOLKIT [45] and

uses the CARPET [46] module for mesh refinement. Each simulation has a resolution labeled `nXY`, where the grid spacing of the refinement level at which the waveform is extracted is specified as  $M/X.YY$ . For example, `n120` corresponds to a grid spacing of  $M/1.2$ .

Only simulations with a resolution label of `n120` or higher are included from the RIT catalog. The simulations were read directly from publicly available strain data files [47].

### 3. MAYA Catalog

The simulations in the MAYA catalog use the MAYA code [25]. Similar to LAZEV, the MAYA code uses the CACTUS/CARPET/EINSTEINTOOLKIT infrastructure for its simulations. It constructs initial data based on the Bowen-York extrinsic curvature, conformally flat spatial metric, and the TWO-PUNCTURES solver. The PN equations of motion are also used to define the initial spins and orbital momentum. MAYA uses the Baumgarte-Shapiro-Shibata-Nakamura [41, 42] formulation to evolve the initial data, employing mesh refinement for higher-resolution simulations.

The publicly available MAYA data files [48] were read using the `mayawaves` [49] Python package.

### 4. Selection criteria

The linear shift in the time origin of the coordinates, which arises from the residual motion of the center of mass of the binary system [50], was corrected for all simulations used. Additionally, all simulations are selected to have initial orbital eccentricities of less than 0.002, as reported by their respective catalogs.<sup>4</sup>

For nonspinning binary systems, simulations with any mass ratio are included, provided that the initial magnitude of each of the six dimensionless spin components is less than  $10^{-4}$ . Table I in Appendix A lists the nonspinning simulations used in this work.

For aligned-spin binary systems, simulations with fixed mass ratios  $q \in \{1.0, 1.5, 2.0\}$  are used. The initial perpendicular components of the dimensionless spins are required to be less than  $10^{-4}$ . Additionally,  $\chi_i \geq 0.1$  for at least one of the black holes to enhance the impact of spins on the waveforms. Table II lists the aligned-spin simulations used from the SXS, RIT, and MAYA catalogs.

We refer to the selected simulations as *datasets* for each NR catalog. After extracting the mode amplitudes  $\hat{A}_{\ell m}$  from each dataset, their dependence on the

binary parameters was modeled using fits motivated by the leading-order PN dependence.

## C. Post-Newtonian Expansion

The PN approximation describes the motion of inspiraling compact binaries and their emission of GWs [6]. It is an expansion in the characteristic internal velocity  $v$  of the system, making the approximation valid for sources that are slowly moving and weakly stressed. Several works [6, 27, 52, 53] have computed the complex  $h_{\ell m}$  modes at various PN expansion orders. The expressions for the relative mode amplitudes  $\hat{A}_{\ell m}$  referenced throughout this work are shown in Appendix B and can be obtained from Refs. [6, 27, 52–54].

For nonspinning binaries, we focus on modes with  $\ell \leq 4$  and  $0 < m \leq \ell$ .<sup>5</sup> Among these, the  $(2, 2)$ ,  $(2, 1)$ ,  $(3, 3)$ , and  $(4, 4)$  modes are generally the strongest [55].

For aligned-spin systems, we consider the modes  $\{(\ell, m)\} = \{(2, 1), (3, 2), (4, 3), (4, 1)\}$ . This is because  $\ell + m = \text{odd}$  modes are the current multipole moments, which are directly related to the system’s total angular momentum [6]. Spin effects are not present at leading order for any mode, but current-multipole modes contain spin-dependent terms at next-to-leading order and are therefore more likely to exhibit spin effects.

## D. Investigating the leading-order post-Newtonian dependence

We examine how the GW mode amplitudes vary with the mass ratio and spins of the system over a range of times using fit ansätze that are motivated by PN theory. Near the merger, the PN approximation breaks down. However, Ref. [11] suggested that the leading order dependence of the mode amplitudes on the intrinsic parameters persists through the merger. The first objective of this study is to derive and reinterpret these results by directly fitting for  $v$  in the PN expressions at each time step.

Following Ref. [11], a fit is constructed for each mode based on the leading-order functional form of the PN expressions (see Appendix B). Instead of fitting for an overall factor, we directly replace powers of  $v$  with independent fit coefficients. The fit coefficient that replaces the  $v^n$  term in  $\hat{A}_{\ell m}$  is denoted  $a_{\ell m}^{(n)}$ . At early times, these PN-inspired models should recover approximately consistent fit coefficients across modes. At late times, the recovered fit coefficients can be expected to diverge between modes, even if the fits accurately describe the data,

<sup>4</sup> Eccentricity is not consistently defined across catalogs. While there are methods [51] for consistently calculating eccentricity using waveform data, reevaluating the eccentricity for all simulations considered here is beyond the scope of this work.

<sup>5</sup> Nonprecessing systems exhibit mirror symmetry, meaning that the  $-m$  modes are fully determined by the positive- $m$  modes through the relation  $h_{\ell, -m} = (-1)^{\ell} h_{\ell m}^*$ . For this reason, we focus only on modes with  $m > 0$ .

as each absorbs different higher-order corrections beyond the leading-order PN prediction.

### 1. Leading-order fits for nonspinning simulations

For nonspinning simulations, the resulting leading-order fitting functions are:

$$\hat{A}_{22}^{(\text{LO})} = 8\sqrt{\frac{\pi}{5}} \eta a_{22}^{(2)}, \quad (7a)$$

$$\hat{A}_{21}^{(\text{LO})} = \frac{1}{3} \delta a_{21}^{(1)}, \quad (7b)$$

$$\hat{A}_{33}^{(\text{LO})} = \frac{3}{4} \sqrt{\frac{15}{14}} \delta a_{33}^{(1)}, \quad (7c)$$

$$\hat{A}_{32}^{(\text{LO})} = \frac{1}{3} \sqrt{\frac{5}{7}} (1 - 3\eta) a_{32}^{(2)}, \quad (7d)$$

$$\hat{A}_{31}^{(\text{LO})} = \frac{\delta}{12\sqrt{14}} a_{31}^{(1)}, \quad (7e)$$

$$\hat{A}_{44}^{(\text{LO})} = -\frac{8}{9} \sqrt{\frac{5}{7}} (3\eta - 1) a_{44}^{(2)}, \quad (7f)$$

$$\hat{A}_{43}^{(\text{LO})} = \frac{9\delta(1-2\eta)}{4\sqrt{70}} a_{43}^{(3)}, \quad (7g)$$

$$\hat{A}_{42}^{(\text{LO})} = \frac{\sqrt{5}}{63} (1 - 3\eta) a_{42}^{(2)}, \quad (7h)$$

$$\hat{A}_{41}^{(\text{LO})} = \frac{\delta(1-2\eta)}{84\sqrt{10}} a_{41}^{(3)}. \quad (7i)$$

$$(7j)$$

To perform the fits, we extract  $\hat{A}_{\ell m}$  from the NR simulation at each time step and apply the fitting functions presented above. This procedure yields a set of time-dependent fit coefficients  $a_{\ell m}^{(n)}(t)$ , which enable us to track their evolution and physical significance.

Since each NR catalog contains a sufficient number of nonspinning simulations that satisfy the selection criteria, the fits can be meaningfully applied to each dataset individually. We apply the fits to the individual catalogs and to the joint dataset to assess their consistency.

### 2. Leading-order fits for aligned-spin simulations

For aligned-spin systems, the resulting fits are:

$$\hat{A}_{21}^{(\text{LO},S)} = \left| \hat{A}_{21}^{\text{ns}} - \frac{1}{2} (\chi_a + \delta\chi_s) a_{21}^{(2)} \right|, \quad (8a)$$

$$\hat{A}_{32}^{(\text{LO},S)} = \left| \hat{A}_{32}^{\text{ns}} + \frac{4}{3} \sqrt{\frac{5}{7}} \eta \chi_s a_{32}^{(3)} \right|, \quad (8b)$$

$$\hat{A}_{43}^{(\text{LO},S)} = \left| \hat{A}_{43}^{\text{ns}} + \frac{45}{8\sqrt{70}} \eta (\chi_a - \delta\chi_s) a_{43}^{(4)} \right|, \quad (8c)$$

$$\hat{A}_{41}^{(\text{LO},S)} = \left| \hat{A}_{41}^{\text{ns}} + \frac{5}{84\sqrt{40}} \eta (\delta\chi_s - \chi_a) a_{41}^{(4)} \right|. \quad (8d)$$

where  $\hat{A}_{\ell m}^{\text{ns}}$  is the  $(\ell, m)$  mode amplitude of a nonspinning system with the corresponding mass ratio. The amplitude data is extracted at each time step from aligned-spin simulations with fixed mass ratios  $q = \{1.0, 1.5, 2.0\}$ . With the time and mass ratio fixed, the amplitudes are treated as functions of  $(\chi_{1z}, \chi_{2z})$ , and the fits above are applied.

In Ref. [11], the authors obtained results for aligned-spin systems separately from those for nonspinning systems. However, suppose the leading-order spin combination (e.g.,  $\chi_a + \delta\chi_s$  for the  $(2, 1)$  mode) truly governs the mode's spin dependence through the merger. Whenever this effective spin combination vanishes, the amplitude should then closely match that of a nonspinning system with the same mass ratio. Therefore, to fully isolate the spin dependence, we set  $\hat{A}_{\ell m}^{\text{ns}}$  in the above fits to the NR amplitudes from SXS:BBH:4434 when  $q = 1.0$ , SXS:BBH:3984 when  $q = 1.5$ , and SXS:BBH:2497 when  $q = 2.0$ .

### E. Introducing higher-order dependencies

In previous work, the amplitudes of several modes, most notably the  $(3, 2)$  mode, but also the  $(3, 1)$ ,  $(4, 3)$ ,  $(4, 2)$ , and  $(4, 1)$  modes, exhibited deviations from the leading-order PN fits at late times [11]. The second objective of this study is to develop improved models for the relative mode amplitudes by incorporating higher-order dependencies on the intrinsic parameters.

#### 1. Higher-order fits for nonspinning simulations

We construct fitting functions for the relative mode amplitudes of nonspinning systems that incorporate higher-order dependencies on the symmetric mass ratio  $\eta$ . Our primary focus in this section is on the quality of the fit, rather than the physical interpretation of the coefficients. Therefore, we do not explicitly replace powers of  $v$  with a fit coefficient. Instead, we allow the coefficients to absorb all overall factors and velocity dependencies, and we determine which modes and times are better described with these higher-order fits.

By inspection of the PN expressions in Appendix B, we observe that for modes with even  $m$ , higher-order PN terms introduce higher powers of  $\eta$ . In modes with odd  $m$ , the amplitudes additionally acquire an overall factor of  $\delta$ . Thus, we define a family of higher-order fitting functions  $\hat{A}_{\ell m}^{(N)}$  as follows:

$$\hat{A}_{\ell m}^{(N)} = \begin{cases} \sum_{i=0}^N c_i \eta^i, & \text{for even } m \\ \delta \sum_{i=0}^N c_i \eta^i, & \text{for odd } m. \end{cases} \quad (9)$$

These fits allow us to determine the minimum degree of higher-order dependencies needed to model deviations from leading-order fits.

## 2. Higher-order fits for aligned-spin simulations

Similarly, for aligned-spin systems, we define higher-order fitting functions that incorporate linear and quadratic dependencies on  $\chi_s$  and  $\chi_a$ :

$$\hat{A}_{\ell m}^{(1,S)} = \hat{A}_{\ell m}^{\text{ns}} + \sum_{i=a,s} c_i \chi_i, \quad (10a)$$

$$\hat{A}_{\ell m}^{(2,S)} = \hat{A}_{\ell m}^{\text{ns}} + \sum_{i=a,s} c_i \chi_i + \sum_{i=a,s} \sum_{j=a,s} c_{ij} \chi_i \chi_j. \quad (10b)$$

As done with the leading-order fits, we fix the mass ratio and use the nonspinning NR reference amplitudes  $\hat{A}_{\ell m}^{\text{ns}}$ .

## F. Fitting procedure

The optimal fit coefficients are obtained using SciPy's `differential_evolution` algorithm. This global optimization method evolves a population of candidate solutions to minimize a given cost function [56]. We set the cost function to the sum of squared residuals between the fit and the NR data. We constrain the leading-order fit coefficients to the interval  $[-5, 5]$  and higher-order coefficients to  $[-1, 1]$ , based on empirical observations of their typical magnitudes during preliminary fits.

The quality of each fit is evaluated using the Pearson correlation coefficient,

$$C_{\ell m} = \frac{(\hat{A}_{\ell m}^{(\text{fit})} - \bar{A}_{\ell m}^{(\text{fit})}) \cdot (\hat{A}_{\ell m}^{(\text{NR})} - \bar{A}_{\ell m}^{(\text{NR})})}{\sqrt{(\hat{A}_{\ell m}^{(\text{fit})} - \bar{A}_{\ell m}^{(\text{fit})})^2 (\hat{A}_{\ell m}^{(\text{NR})} - \bar{A}_{\ell m}^{(\text{NR})})^2}}, \quad (11)$$

where  $\hat{A}_{\ell m}^{(\text{fit})}$  represents the predicted amplitude values from the fitting functions, and  $\hat{A}_{\ell m}^{(\text{NR})}$  is the reference amplitude data obtained from NR simulations. Overbars denote the mean values of the datasets.

Fits are considered stable if the recovered parameters and the Pearson correlation coefficient vary smoothly over time.

## III. RESULTS AND DISCUSSION

### A. Stability and time evolution of leading-order PN-inspired fits

#### 1. Nonspinning simulations

Fig. 2 shows the optimal fit parameters obtained for the leading-order models defined in Eqs. 7 over the time interval considered, using individual catalogs and the

joint dataset. To directly compare the fit coefficients, the figure shows  $\sqrt[n]{a_{\ell m}^{(n)}}$ , so that all parameters correspond to fitting for  $v$  at early times. The Pearson correlation coefficient is also shown as a function of time for each mode to quantify the agreement between the data and the fits.

For the (2, 2), (2, 1), (3, 3), (3, 2), (4, 4), and (4, 3) modes, all catalogs recover similar values for the fit coefficients. The fits maintain a Pearson correlation above 0.99 at all times for the (2, 2), (2, 1), and (3, 3) modes across catalogs, except briefly for MAYA, which contributed the fewest simulations to our data set. MAYA simulations also exhibit fluctuations at earlier times for the (4, 4) mode.

For the weaker modes, there is significantly more variability across catalogs. The SXS dataset, which contributed the most simulations to our full dataset, showed the greatest stability. It is followed by the RIT dataset, which shows instabilities only for the (4, 2) and (4, 1) modes, but otherwise performs similarly to the SXS dataset. The MAYA dataset is stable for the (3, 2) and (4, 3) modes, but unstable for the (3, 1), (4, 2) and (4, 1) modes. These subdominant modes have lower amplitudes and are more susceptible to numerical errors. Additionally, higher- $\ell$  modes have higher frequencies and more complex sourcing, making them more susceptible to resolution-dependent differences [19, 31].

Focusing on the joint dataset, the recovered fit coefficients yield approximately consistent numerical values at early times across modes, though they are not identical. These differences reflect the limitations of the leading-order PN approximation even at the earliest time considered ( $t = -500M$ ). The fit coefficients must absorb corrections from higher-order PN terms, albeit these corrections are smaller at earlier times.

Once a common horizon forms, the velocity parameter  $v$  becomes ill-defined, and the fit coefficients need not be approximately consistent across modes. The coefficients tend to grow as each mode absorbs increasingly significant higher-order corrections. For example, the (2, 1) mode exhibits a large increase, indicating that this mode absorbs substantial higher-order corrections that are well-described by the  $\eta$ -dependence in Eq. 7b.

Focusing on the results for the SXS dataset, which shows the smoothest behavior, we find that the fits remain accurate for all modes throughout most of their evolution. However, the quality drops sharply beyond  $t = 0M$  for all weaker modes. This decline indicates that higher-order corrections introduce markedly different dependencies on  $\eta$  that cannot be captured by the leading-order basis alone, and additional  $\eta$  dependencies must be introduced.

#### 2. Aligned-spin simulations

To reduce the impact of cross-catalog differences, we performed fits on the aligned-spin simulations using only

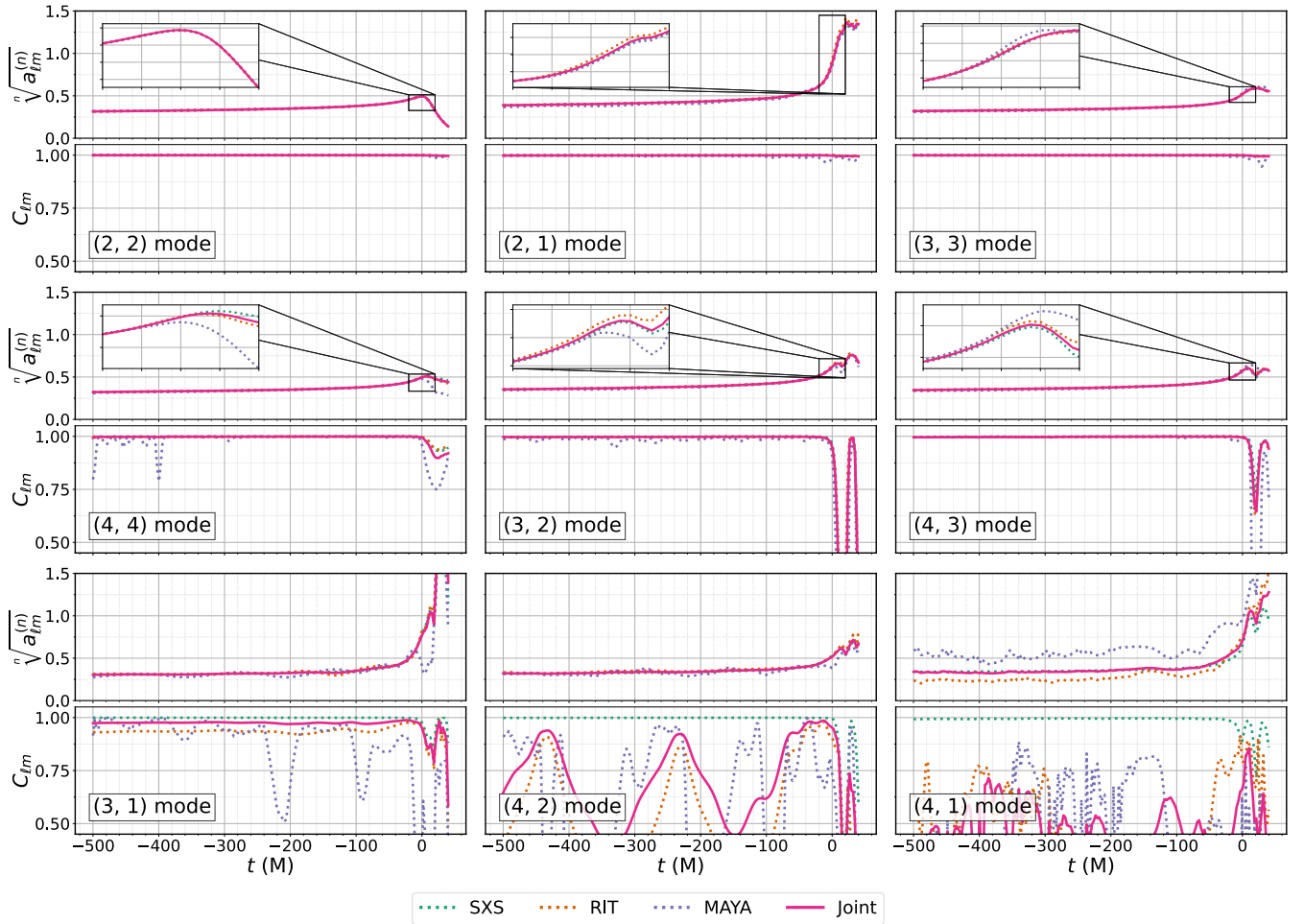


FIG. 2. *Leading-order fits for nonspinning simulations*: Optimal fit coefficients  $\sqrt[n]{a_{\ell m}^{(n)}}$  and Pearson correlation  $C_{\ell m}$  for the leading-order fits defined in Eqs. 7, shown as a function of time  $t$  after the peak of the (2,2) mode. The dashed curves show results obtained from each individual catalog, while the solid curve shows results obtained from the joint dataset. Insets highlight cross-catalog differences in fit coefficients for  $t \in (-20M, 20M)$ . At early times, the coefficients fit the PN velocity  $v$ , whereas at late times they absorb higher-order corrections.  $C_{\ell m}$  quantifies the quality of these fits in capturing such corrections.

the SXS dataset. Nonetheless, Appendix C presents snapshots of the SXS fits with RIT and MAYA data included for visual comparison across catalogs. These fit snapshots are also available as interactive 3D plots in Ref. [57].

Fig. 3 shows the fit parameters over time. Early on, recovered parameters vary little across mass ratios. This is because higher-order corrections depending solely on mass ratio are accounted for by the nonspinning NR amplitudes  $\hat{A}_{\ell m}^{(\text{ns})}$  used in the fits. The consistency across mass ratios up to  $t \approx -20M$  indicates that higher-order spin corrections introduce little to no additional mass-ratio dependence, beyond that captured at leading order. However, differences become more pronounced after the merger, where higher-order spin effects with distinct mass-ratio dependencies play a more significant role.

Regarding fit quality, the (2,1) mode remains well-described by leading-order spin dependence beyond

merger, consistent with [11]. The (3,2) mode deviates from the PN dependence around  $t \approx 0M$ , especially at higher mass ratios, but performs well again at  $t \approx 30M$ . The (4,3) fit performs well for  $q = 1.0$ , but breaks down post-merger at higher mass ratios. The (4,1) fit also performs well for  $q = 1.0$  up to  $t \approx 0M$ , and performs poorly for higher mass ratios, which is evident in the Figs. 7–9 in Appendix C. The result in [11] found better agreement for higher mass ratios in the (4,1) mode. However, their analysis allowed a constant offset to vary freely, whereas we fixed this offset by enforcing the nonspinning limit through our  $\hat{A}_{\ell m}^{(\text{ns})}$ . This suggests that some higher-order spin effects were possibly absorbed into their constant offset and may not be captured in our approach.



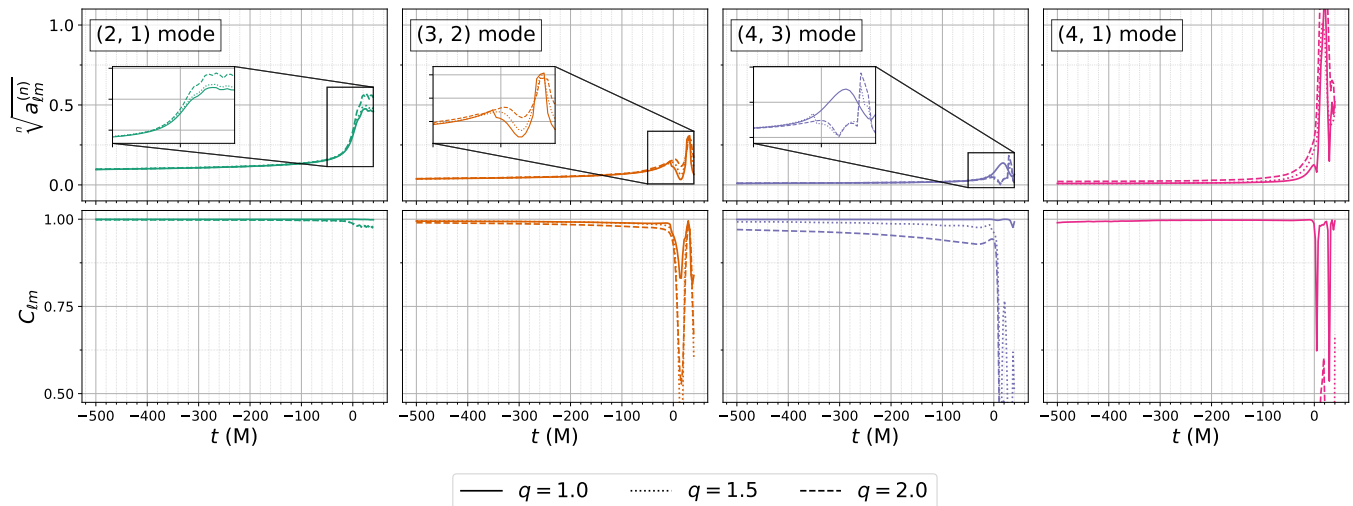


FIG. 3. *Leading-order fits for aligned-spin simulations*: Optimal fit coefficients  $\sqrt[n]{a_{\ell m}^{(n)}}$  and Pearson correlation  $C_{\ell m}$  for the leading-order fits defined in Eqs. 8, shown as a function of time  $t$  after the peak of the (2,2) mode. All fits were performed using simulations from the SXS catalog only. At early times, the coefficients fit the PN velocity  $v$ , whereas at late times they absorb higher-order corrections.  $C_{\ell m}$  quantifies the quality of these fits in capturing such corrections. Line styles correspond to different mass ratios. An inset is not included for the (4, 1) mode due to its unstable behavior around  $t = 0M$ .

## B. Higher-order fits

We now investigate the extent to which higher-order dependencies are needed to significantly improve fit quality for nonspinning and aligned-spin simulations.

### 1. Nonspinning simulations

The impact of higher-order corrections on the quality of fits for nonspinning systems is illustrated in two complementary figures. Fig. 4 shows the Pearson correlation coefficients for each mode obtained when applying fits of different degrees  $N$ , while Fig. 5 provides snapshots of the amplitude data and their corresponding fits at selected times. Together, these figures allow for a direct visual assessment of how the inclusion of higher-order terms improves modeling accuracy across modes and times.

At early times ( $t \ll 0$ ), higher-order corrections have little effect on fit quality. In this regime, corrections from higher-order  $\eta$  dependencies are small and are effectively absorbed by the leading-order PN term. This behavior is expected, as leading-order fits were already found to perform well across all modes at early times in both prior work and the results presented in the previous section.

As the system approaches merger ( $t \rightarrow 0$ ), and especially in the post-merger regime ( $t > 0$ ), higher-order dependencies become increasingly relevant, leading to noticeable improvements in fit quality for several modes. This behavior is captured in both the time evolution of correlation coefficients and the data snapshots. We observe the following trends:

- **(2, 2) mode**: The leading-order PN fit, captured by

$N = 1$ , remains accurate through the merger. The differences between  $N = 2$  and  $N = 3$  are minimal, confirming that this mode is well described by a linear dependence on  $\eta$ .

- **(2, 1) and (3, 3) modes**: These modes, whose leading-order behavior corresponds to  $N = 0$ , benefit from the inclusion of a linear term in  $\eta$ . Improvements are particularly noticeable after the merger, as seen in Fig. 5. However, improvements beyond  $N = 1$  are minimal, suggesting that  $N = 1$  fits are sufficient for modeling this mode.
- **(4, 4) mode**: Higher-order terms become significantly more important after the merger. The  $N = 3$  fit shows a clear advantage over lower-order models in this regime. Notably, while the Pearson correlation for the fits dips at  $t \approx 0$ , the snapshot at  $t = -0.70M$  shows that the models still accurately capture the amplitude structure around this time.
- **Subdominant modes with  $\ell = 3, 4$  and  $m < \ell$** : These modes, previously identified as poorly-described by leading-order PN predictions, show a strong preference for higher-order fits near and beyond the merger. Nevertheless, our low-degree polynomial fits can capture their amplitude evolution with accuracy comparable to the fits for the stronger modes. The improvements are apparent at late times in the snapshots in Fig. 5.

Fig. 5 also plots data points from the RIT and MAYA catalogs. Although these were not used to generate the fits, they generally align well with the SXS-based fits.



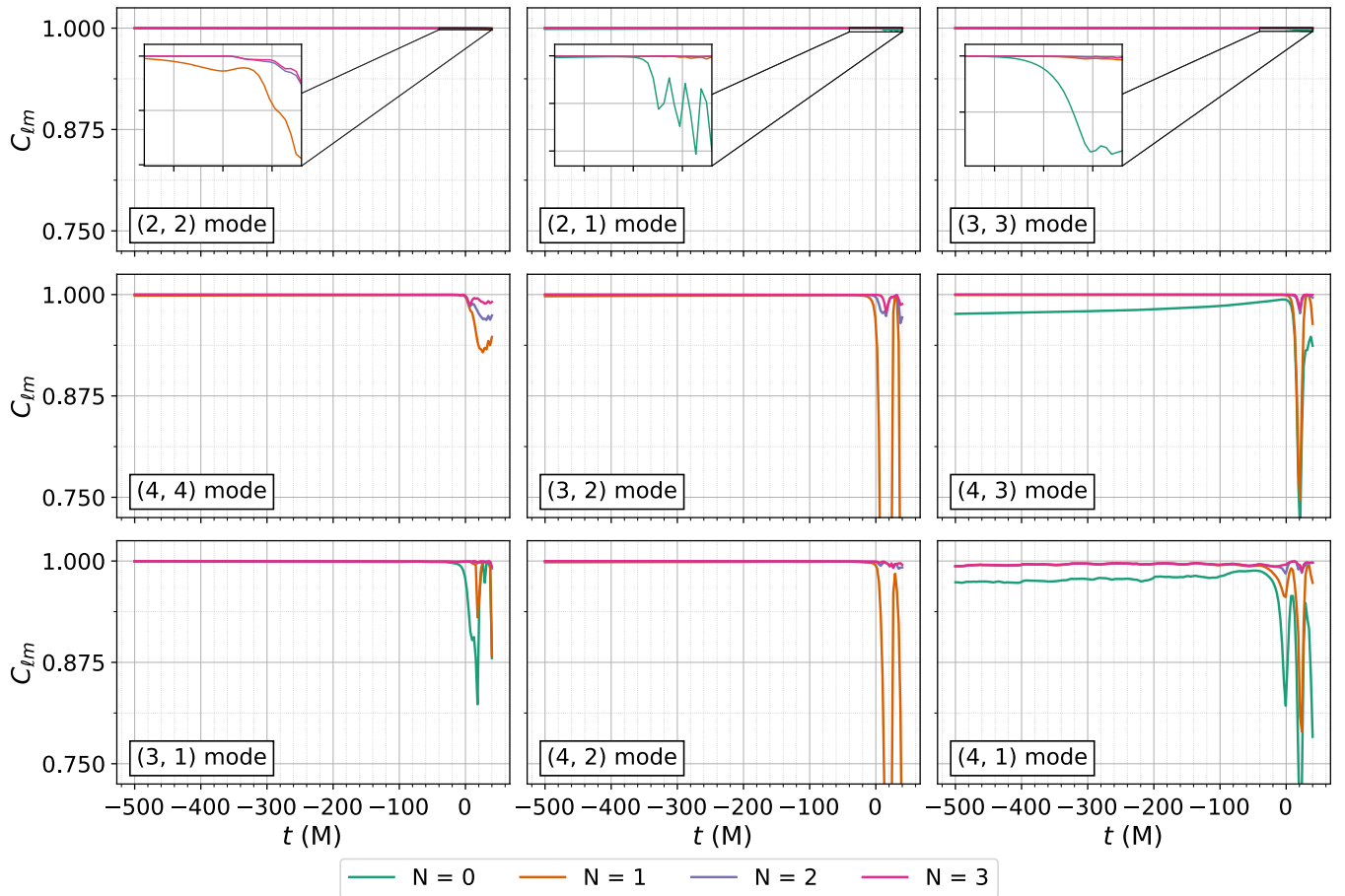


FIG. 4. *Higher-order fits for nonspinning simulations*: Pearson correlation coefficient for each model in the higher-order family defined in Eq. (9), shown as a function of time  $t$  after the peak of the (2,2) mode. Including higher-order dependencies generally improves fit quality, especially for subdominant modes after  $t \approx 0$ .

However, cross-catalog dispersion increases at later times for subdominant modes, particularly for the (4,2) and (4,1) modes.

## 2. Aligned-spin simulations

Fig. 6 shows the Pearson correlation of the higher-order aligned-spin fits  $\hat{A}_{lm}^{(i,S)}$  defined in Eq. 10 for each mode across time, with the corresponding values from the leading-order fits included for reference. To further illustrate the behavior of the fits, Figs. 7–9 present snapshots of the amplitude data and their associated fits at selected times for different mass ratios. These snapshots are also available as interactive 3D plots in Ref. [57].

The quadratic fits occasionally show instabilities, especially for higher mass ratios, likely due to degeneracies among the five fit coefficients and relatively sparser coverage of simulations. In cases where the quadratic fits result in a lower Pearson correlation than the corresponding linear fits, we retain the linear fit parameters  $c_a$  and  $c_s$  and set all quadratic coefficients  $c_{ss}, c_{aa}, c_{as}$  to zero.

These instabilities are notable in Fig. 6, where the Pearson correlation for the quadratic fit intermittently drops to that of the linear fit.

For  $q = 1.0$  simulations, the linear fit performs almost identically to the leading-order fit across all modes. The quadratic fit has little impact on fit quality, with the exception of the (3,2) mode, where it significantly improves the correlation. This improvement is also visually evident in Fig. 7.

For higher mass ratios, the (2,1) mode benefits from the additional flexibility of the higher-order fits only very close to and after the merger. On the other hand, the (3,2) mode consistently shows substantial improvement with the inclusion of quadratic terms, which can also be corroborated visually in Figs. 7–9. For the (4,3) mode, the advantage of higher-order fits becomes more pronounced as the mass ratio increases. Finally, the (4,1) mode shows erratic behavior throughout, especially after the merger, which we attribute to numerical noise affecting this mode.

Overall, the inclusion of quadratic spin terms improves the modeling of the (3,2) mode for all mass ratios consid-

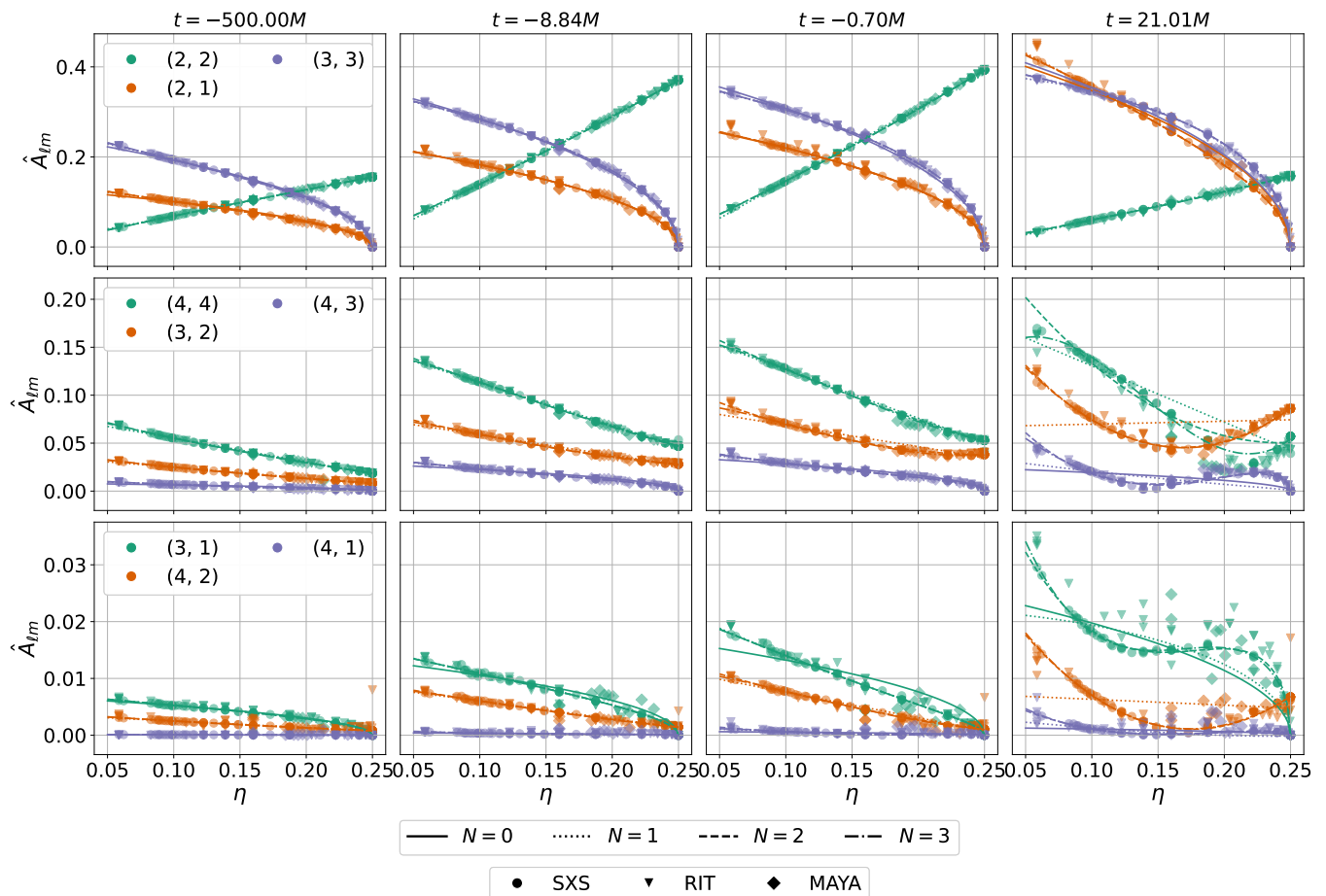


FIG. 5. *Higher-order fit snapshots for nonspinning simulations*: Snapshots of the  $(\ell, m)$ -mode amplitudes, normalized to the  $(2, 2)$  mode, at selected times  $t$  relative to the peak of the  $(2, 2)$  mode, as a function of the symmetric mass ratio  $\eta$ . Line styles correspond to polynomial fits in  $\eta$  at different orders  $N$ , as defined in Eq. (9). Colors indicate the modes displayed in each row, and markers denote the NR catalog associated with each data point. The best-fit curves shown were obtained using data from the SXS catalog only.

ered and of the  $(4, 3)$  mode for mass ratios  $q > 1$  after the merger. Visual comparison of the RIT and MAYA simulations in Figs. 7–9 confirms cross-catalog consistency with these improved higher-order fits for the  $(2, 1)$ ,  $(3, 2)$ , and  $(4, 3)$  modes. For the  $(4, 1)$  mode, however, there is greater dispersion across catalogs, again likely due to numerical resolution differences.

#### IV. CONCLUSIONS

In this study, we analyzed the mode amplitudes of quasi-circular, nonprecessing BBH mergers using NR data. Our primary goal was to understand the extent to which the PN dependence on mass ratios and spins is carried over from the inspiral, particularly near and after the merger, where modeling remains challenging.

We obtained fit coefficients for the mode amplitudes relative to the  $(2, 2)$  mode as a function of time and verified their stability across the waveform, from late-

inspiral ( $t = -500M$ ) to post-merger ( $t = +40M$ ). The stability and quality of these fits demonstrate that for several modes, the time dependence can be cleanly separated from the dependence on the mass ratio and spin. This separation provides a framework for constructing simplified waveform models in the near- and post-merger regime by directly modeling the time evolution of the fit coefficients.

In the late-inspiral region, we connected the fit coefficients to the PN velocity. As the system evolves toward the merger, the coefficients deviate from the PN predictions, but we interpret these deviations as absorptions of higher-order effects that preserve the same overall dependence on mass ratio and spin. This reinterpretation provides intuition behind why these PN-inspired fits can be applied in the strong-field regime.

To explore higher-order parameter dependencies, we tested fits of increasing complexity in both mass ratio and spin. For nonspinning systems, we found that PN-inspired fits with polynomial order  $N \leq 3$  are sufficient

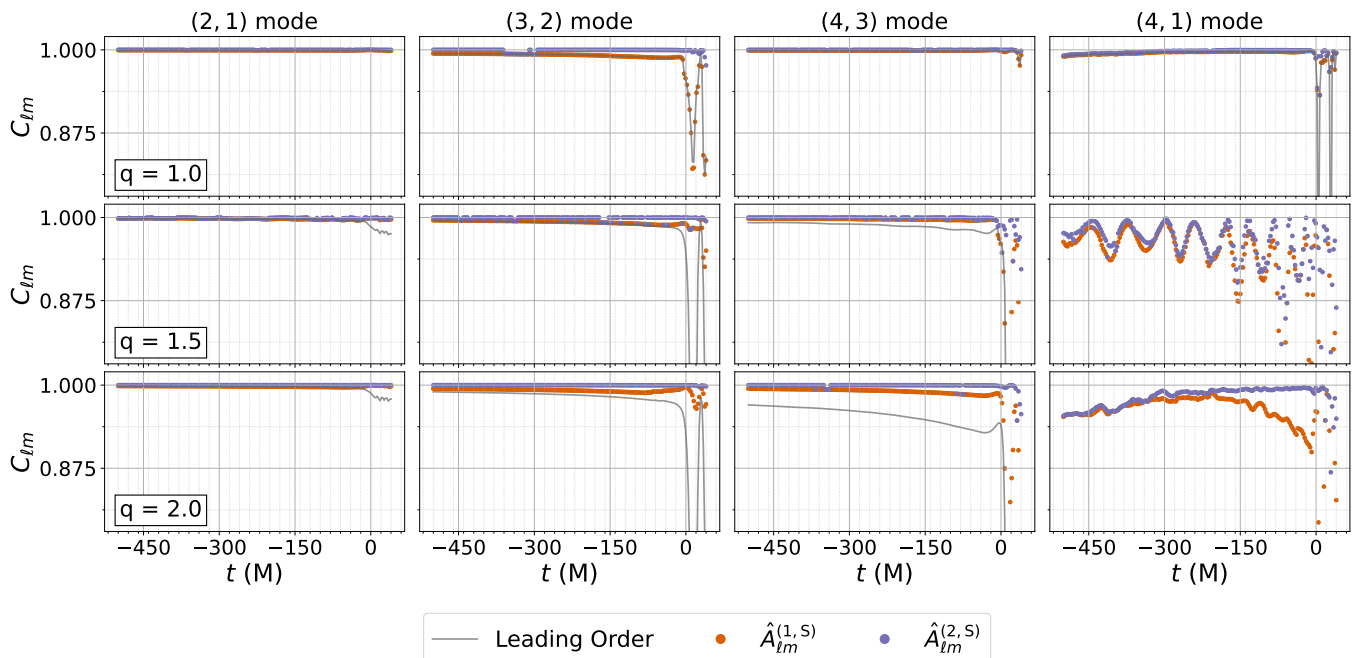


FIG. 6. *Higher-order fits for aligned-spin simulations:* Pearson correlation  $C_{\ell m}$  as a function of time  $t$  relative to the peak of the (2,2) mode for different models: the leading-order (gray) fits defined in Eq. 8, and the linear (orange) and quadratic (purple) fits defined in Eqs. 10. Results for different mass ratios considered are shown in separate rows. All fits are obtained using data from the SXS catalog only.

to model relative mode amplitudes accurately even close to the merger. While leading-order fits remain effective through the late-inspiral, selectively incorporating higher-order terms substantially improves the modeling of subdominant modes near and after the merger. For aligned-spin simulations, we found that quadratic fits in  $\chi_s$  and  $\chi_a$  offer notable improvements for modes that were not well-modeled by the leading-order PN fits, such as the (3,2) mode. However, the large number of free parameters in quadratic fits can lead to instabilities, highlighting a tradeoff between flexibility and robustness.

We validated these results across the SXS, RIT, and MAYA catalogs. While several fits were performed using only SXS data, we generally found good agreement with the other catalogs. Discrepancies in a small number of cases may point to waveform inconsistencies or numerical artifacts and can serve as indicators of outlying simulations.

In future work, we aim to extend this analysis to simulations of precessing systems. Overall, this study advances the understanding of mode amplitude structure in BBH mergers and lays a framework for efficient amplitude-consistent waveform modeling, particularly near the merger.

## ACKNOWLEDGMENTS

We wish to acknowledge B. S. Sathyaprakash for his invaluable guidance and insightful comments throughout this work. We thank the SXS, RIT, and MAYA collaborations for their publicly available catalogs of NR simulations used in this study. We also thank Vaishak Prasad for his assistance with the SXS catalog, Carlos Lousto for guidance using the RIT catalog, and Deborah Ferguson for help with using `mayawaves` and the MAYA catalog. We are also grateful to Ssohrab Borhanian for answering questions related to his original study and to Koustav Chandra, Rossella Gamba, and Dongze Sun for helpful discussions.

## Appendix A: Selected simulations

Tables I and II list the simulations from the SXS, RIT, and MAYA catalogs that were used in this study, following the selection criteria outlined in Section II B. Table I lists the nonspinning simulations with their mass ratio, while Table II lists the aligned-spin simulations with their mass ratio and dimensionless spin components.

## Appendix B: Post-Newtonian expressions for relative mode amplitudes

The PN waveform mode amplitudes *relative to the* (2,2) mode up to  $\mathcal{O}(v^5)$  are given by [6]:

TABLE I. List of 107 nonspinning simulations from the SXS, RIT, and MAYA catalogs used in this work, grouped by mass ratio  $q$ .

$q$	ID(s)	$q$	ID(s)	$q$	ID(s)
1.00	SXS:BBH:0389, SXS:BBH:2377, SXS:BBH:2378, SXS:BBH:3624, SXS:BBH:4434, SXS:BBH:2496, SXS:BBH:1132, SXS:BBH:3864, SXS:BBH:1154, SXS:BBH:1155, SXS:BBH:1153, SXS:BBH:3617, SXS:BBH:2375, SXS:BBH:3634, SXS:BBH:2376, SXS:BBH:2325, SXS:BBH:2326, RIT:BBH:0112, RIT:eBBH:1090	1.08	RIT:BBH:0458	1.18	RIT:BBH:0084, RIT:BBH:0113
1.20	SXS:BBH:0198	1.33	RIT:BBH:0045, RIT:BBH:0114, RIT:eBBH:1241	1.50	SXS:BBH:2331, SXS:BBH:3984, SXS:BBH:0593, RIT:BBH:0085, RIT:BBH:0115
1.67	RIT:BBH:0086, RIT:BBH:0116	1.75	GT0727	1.82	RIT:BBH:1020
2.00	SXS:BBH:2497, SXS:BBH:1166, SXS:BBH:1167, RIT:BBH:0077, RIT:BBH:0117, RIT:eBBH:1200, GT0446	2.25	GT0757	2.32	SXS:BBH:0201
2.41	RIT:BBH:0139	2.50	RIT:BBH:0087, RIT:BBH:0118	2.60	GT0651
2.70	GT0650	2.80	GT0653	2.90	GT0654
3.00	SXS:BBH:1178, SXS:BBH:1179, SXS:BBH:2498, SXS:BBH:2265, RIT:BBH:0102, RIT:BBH:0138	3.10	GT0758	3.50	SXS:BBH:2483
4.00	SXS:BBH:2485, SXS:BBH:3631, SXS:BBH:2499, SXS:BBH:1220, RIT:BBH:0088, RIT:BBH:0119, RIT:eBBH:1133, GT0454, MAYA1040	4.50	SXS:BBH:2484, SXS:BBH:3144	5.00	SXS:BBH:2374, SXS:BBH:2487, SXS:BBH:3619, RIT:BBH:0089, RIT:BBH:0120, RIT:BBH:0152
5.50	SXS:BBH:2486	6.00	SXS:BBH:2164, SXS:BBH:2489, SXS:BBH:3630, RIT:BBH:0090, RIT:BBH:0121	6.50	SXS:BBH:2488
6.58	SXS:BBH:0192	7.00	SXS:BBH:2491, RIT:BBH:0416	7.19	SXS:BBH:0188
7.50	SXS:BBH:2490	7.76	SXS:BBH:0195	8.00	SXS:BBH:2493, SXS:BBH:2707, SXS:BBH:3622
8.27	SXS:BBH:0186	8.50	SXS:BBH:2492	8.73	SXS:BBH:0199
9.00	SXS:BBH:2495	9.17	SXS:BBH:0189	9.20	SXS:BBH:1108
9.50	SXS:BBH:2494	9.99	SXS:BBH:0185	10.00	RIT:BBH:0978
14.00	SXS:BBH:2480	15.00	SXS:BBH:2477, RIT:BBH:0373, RIT:BBH:0942, RIT:BBH:0943, RIT:BBH:0957		

TABLE II. List of 176 aligned-spin simulations from the SXS, RIT, and MAYA catalogs used in this work. Only SXS simulations were used to construct the fits in Figs.7–9, but RIT and MAYA simulations are included for visual comparison.

$q$	ID	$\chi_{1z}$	$\chi_{2z}$	$q$	ID	$\chi_{1z}$	$\chi_{2z}$	$q$	ID	$\chi_{1z}$	$\chi_{2z}$
1.00	SXS:BBH:2100	0.50	-0.90	1.00	SXS:BBH:2093	-0.50	0.90	1.00	SXS:BBH:1492	-0.47	-0.79
1.00	SXS:BBH:2099	0.40	0.80	1.00	SXS:BBH:2098	0.40	-0.80	1.00	SXS:BBH:2095	-0.40	0.80
1.00	SXS:BBH:2094	-0.40	-0.80	1.00	SXS:BBH:3912	-0.47	-0.79	1.00	SXS:BBH:3982	-0.18	0.72
1.00	SXS:BBH:3923	0.14	0.73	1.00	SXS:BBH:1502	-0.42	0.70	1.00	SXS:BBH:3922	-0.42	0.70
1.00	SXS:BBH:4066	-0.95	0.95	1.00	SXS:BBH:3977	0.95	-0.95	1.00	SXS:BBH:0436	-0.20	-0.40
1.00	SXS:BBH:3534	-0.80	0.80	1.00	SXS:BBH:0304	0.50	-0.50	1.00	SXS:BBH:0459	0.20	-0.40
1.00	SXS:BBH:0370	-0.20	0.40	1.00	SXS:BBH:4029	0.95	-0.95	1.00	SXS:BBH:0327	0.80	-0.80
1.00	SXS:BBH:1124	1.00	1.00	1.00	SXS:BBH:2092	-0.50	0.50	1.00	SXS:BBH:2422	0.60	0.60
1.00	SXS:BBH:2419	-0.20	-0.20	1.00	SXS:BBH:2418	-0.44	-0.44	1.00	SXS:BBH:4072	-0.95	-0.95
1.00	SXS:BBH:3629	-0.90	-0.90	1.00	SXS:BBH:1475	-0.80	-0.80	1.00	SXS:BBH:2102	0.60	0.60
1.00	SXS:BBH:1137	-0.97	-0.97	1.00	SXS:BBH:2500	0.25	0.25	1.00	SXS:BBH:0160	0.90	0.90
1.00	SXS:BBH:1122	0.44	0.44	1.00	SXS:BBH:1123	0.50	0.50	1.00	SXS:BBH:2505	0.50	0.50
1.00	SXS:BBH:2089	-0.60	-0.60	1.00	SXS:BBH:2512	0.70	0.70	1.00	SXS:BBH:0178	0.99	0.99
1.00	SXS:BBH:3897	0.80	0.80	1.00	SXS:BBH:0176	0.96	0.96	1.00	SXS:BBH:3895	-0.80	-0.80
1.00	SXS:BBH:3627	0.95	0.95	1.00	SXS:BBH:2086	-0.80	-0.80	1.00	SXS:BBH:1141	-0.44	-0.44
1.00	SXS:BBH:2509	0.60	0.60	1.00	SXS:BBH:3628	0.97	0.97	1.00	SXS:BBH:3518	-0.80	-0.80
1.00	SXS:BBH:3625	-0.80	-0.80	1.00	SXS:BBH:3976	-0.95	-0.95	1.00	SXS:BBH:2420	0.20	0.20
1.00	SXS:BBH:2421	-0.60	-0.60	1.00	SXS:BBH:3896	-0.80	0.80	1.00	SXS:BBH:2423	0.85	0.85
1.00	SXS:BBH:0172	0.98	0.98	1.00	SXS:BBH:3978	0.95	0.95	1.00	SXS:BBH:0329	-0.80	-0.80
1.00	SXS:BBH:3929	-0.24	-0.10	1.00	SXS:BBH:1509	-0.24	-0.10	1.00	SXS:BBH:1506	0.46	-0.32
1.00	SXS:BBH:3917	0.68	0.67	1.00	SXS:BBH:1497	0.68	0.67	1.00	SXS:BBH:3926	0.46	-0.32
1.00	SXS:BBH:0330	-0.80	0.80	1.00	SXS:BBH:2085	-0.90	0.90	1.00	SXS:BBH:2091	-0.60	0.60
1.00	SXS:BBH:1476	-0.80	0.80	1.00	SXS:BBH:2087	-0.80	0.80	1.00	SXS:BBH:3927	0.51	0.29
1.00	SXS:BBH:1507	0.51	0.29	1.00	SXS:BBH:0376	0.60	-0.40	1.00	SXS:BBH:0394	0.60	0.40
1.00	SXS:BBH:0462	-0.60	-0.40	1.00	SXS:BBH:0447	-0.60	0.40	1.00	SXS:BBH:2088	-0.62	-0.25
1.00	SXS:BBH:2103	0.65	0.25	1.00	SXS:BBH:3919	-0.75	0.34	1.00	SXS:BBH:3915	0.78	0.53
1.00	SXS:BBH:3920	-0.77	-0.2	1.00	SXS:BBH:1495	0.78	0.53	1.00	SXS:BBH:3553	0.80	0.40
1.00	SXS:BBH:3582	-0.80	-0.40	1.00	SXS:BBH:3578	-0.80	0.40	1.00	SXS:BBH:1499	-0.75	0.34
1.00	SXS:BBH:3601	0.80	-0.40	1.00	SXS:BBH:1500	-0.77	-0.20	1.00	SXS:BBH:2106	0.90	0.50
1.00	SXS:BBH:2083	-0.90	-0.50	1.50	SXS:BBH:1146	0.95	0.95	1.50	SXS:BBH:0437	-0.20	-0.80
1.50	SXS:BBH:0579	0.40	-0.80	1.50	SXS:BBH:2342	-0.50	0.50	1.50	SXS:BBH:0369	0.60	-0.80
1.50	SXS:BBH:0392	-0.20	0.80	1.50	SXS:BBH:2348	0.50	-0.50	1.50	SXS:BBH:0441	0.60	0.80
1.50	SXS:BBH:0397	-0.80	-0.40	1.50	SXS:BBH:1415	0.50	0.50	1.50	SXS:BBH:0372	0.80	-0.40
2.00	SXS:BBH:0619	0.90	0.90	2.00	SXS:BBH:2113	-0.37	0.85	2.00	SXS:BBH:2126	0.37	-0.85
2.00	SXS:BBH:2122	0.13	0.85	2.00	SXS:BBH:0617	0.50	0.75	2.00	SXS:BBH:2117	-0.13	-0.85
2.00	SXS:BBH:0399	0.20	0.40	2.00	SXS:BBH:0333	0.80	0.80	2.00	SXS:BBH:0618	0.80	0.80
2.00	SXS:BBH:4073	0.90	0.90	2.00	SXS:BBH:4078	0.90	-0.90	2.00	SXS:BBH:4120	-0.90	-0.90
2.00	SXS:BBH:0584	-0.40	-0.40	2.00	SXS:BBH:4115	-0.90	0.90	2.00	SXS:BBH:2107	-0.87	0.85
2.00	SXS:BBH:0354	-0.20	0.40	2.00	SXS:BBH:2108	-0.85	-0.85	2.00	SXS:BBH:0334	-0.80	-0.80
2.00	SXS:BBH:0335	-0.80	0.80	2.00	SXS:BBH:2128	0.60	-0.60	2.00	SXS:BBH:0574	0.40	0.40
2.00	SXS:BBH:2131	0.85	0.85	2.00	SXS:BBH:2132	0.87	-0.85	2.00	SXS:BBH:2109	-0.60	-0.60
2.00	SXS:BBH:2127	0.50	0.50	2.00	SXS:BBH:2114	-0.30	-0.30	2.00	SXS:BBH:2116	-0.30	0.30
2.00	SXS:BBH:2123	0.30	-0.30	2.00	SXS:BBH:0448	0.40	-0.40	2.00	SXS:BBH:2130	0.60	0.60
2.00	SXS:BBH:0554	0.20	-0.40	2.00	SXS:BBH:2111	-0.60	0.60	2.00	SXS:BBH:2112	-0.50	-0.50
2.00	SXS:BBH:2510	0.60	0.60	2.00	SXS:BBH:2506	0.50	0.50	2.00	SXS:BBH:2501	0.25	0.25
2.00	SXS:BBH:0513	0.60	-0.40	2.00	SXS:BBH:0387	-0.60	-0.40	2.00	SXS:BBH:0614	0.75	-0.50
2.00	SXS:BBH:2125	0.30	0.30	2.00	SXS:BBH:0412	-0.20	-0.40	2.00	SXS:BBH:3981	-0.12	-0.65
1.00	RIT:BBH:0016	0.80	-0.80	1.00	RIT:BBH:0261	0.40	-0.85	1.00	RIT:BBH:0499	0.95	-0.95
1.00	RIT:BBH:0228	-0.40	0.85	1.00	RIT:BBH:0324	0.90	0.90	1.00	RIT:BBH:0573	0.95	0.00
1.50	RIT:BBH:0289	0.80	-0.80	1.50	RIT:BBH:0616	0.95	-0.95	1.50	RIT:BBH:0687	0.95	0.95
1.50	RIT:BBH:0788	0.95	0.00	2.00	RIT:BBH:0083	0.50	-0.50	2.00	RIT:BBH:0245	-0.85	0.50
2.00	RIT:BBH:0247	0.85	-0.50	2.00	RIT:BBH:0296	-0.85	-0.50	2.00	RIT:BBH:0314	0.85	0.50
2.00	RIT:BBH:0336	0.00	-0.80	2.00	RIT:BBH:0338	0.00	0.80	2.00	RIT:BBH:0446	0.50	-0.80
2.00	RIT:BBH:0447	-0.25	-0.25	2.00	RIT:BBH:0451	-0.50	0.80	2.00	RIT:BBH:0452	0.25	-0.25
2.00	RIT:BBH:0454	-0.25	0.25	2.00	RIT:BBH:0457	0.25	0.25	2.00	RIT:BBH:0462	0.85	-0.25
2.00	RIT:BBH:0465	-0.85	-0.25	2.00	RIT:BBH:0466	-0.85	0.25	2.00	RIT:BBH:0477	0.85	0.25
2.00	RIT:BBH:0679	0.95	-0.95	2.00	RIT:BBH:0767	0.95	0.95	2.00	RIT:BBH:0782	0.00	0.95
2.00	RIT:BBH:0796	0.95	0.00	1.00	GT0420	0.20	0.20	1.00	GT0546	0.00	0.20
1.00	GT0574	0.10	0.10	1.50	GT0479	0.20	0.20				

$$\hat{A}_{22}^{(\text{PN})} = 8\sqrt{\frac{\pi}{5}}\eta v^2 + \frac{4}{21}\sqrt{\frac{\pi}{5}}\eta(55\eta - 107)v^4 + \mathcal{O}(v^5) \quad (\text{B1a})$$

$$\hat{A}_{21}^{(\text{PN})} = \frac{\delta v}{3} + \frac{1}{252}\delta(163 - 50\eta)v^3 - \frac{1}{3}\pi\delta v^4 + \mathcal{O}(v^5) \quad (\text{B1b})$$

$$\hat{A}_{33}^{(\text{PN})} = \frac{3}{4}\sqrt{\frac{15}{14}}\delta v + \frac{1}{56}\sqrt{\frac{15}{14}}\delta(29\eta - 61)v^3 + \frac{3}{4}\sqrt{\frac{15}{14}}\pi\delta v^4 + \mathcal{O}(v^5) \quad (\text{B1c})$$

$$\hat{A}_{32}^{(\text{PN})} = \frac{1}{3}\sqrt{\frac{5}{7}}(1 - 3\eta)v^2 + \frac{(254 - 5\eta(16\eta + 113))v^4}{378\sqrt{35}} + \mathcal{O}(v^5) \quad (\text{B1d})$$

$$\hat{A}_{31}^{(\text{PN})} = \frac{\delta v}{12\sqrt{14}} - \frac{\delta(83\eta + 5)v^3}{504\sqrt{14}} - \frac{\pi\delta v^4}{12\sqrt{14}} + \mathcal{O}(v^5) \quad (\text{B1e})$$

$$\hat{A}_{44}^{(\text{PN})} = -\frac{8}{9}\sqrt{\frac{5}{7}}(3\eta - 1)v^2 - \frac{4(25\eta(372\eta - 955) + 6568)v^4}{2079\sqrt{35}} + \mathcal{O}(v^5) \quad (\text{B1f})$$

$$\hat{A}_{43}^{(\text{PN})} = \frac{9\delta(1 - 2\eta)v^3}{4\sqrt{70}} + \mathcal{O}(v^5) \quad (\text{B1g})$$

$$\hat{A}_{42}^{(\text{PN})} = \frac{1}{63}\sqrt{5}(1 - 3\eta)v^2 + \frac{(7080\eta^2 + 7495\eta - 3292)v^4}{29106\sqrt{5}} + \mathcal{O}(v^5) \quad (\text{B1h})$$

$$\hat{A}_{41}^{(\text{PN})} = \frac{\delta(1 - 2\eta)v^3}{84\sqrt{10}} + \mathcal{O}(v^5) \quad (\text{B1i})$$

where the total mass and luminosity distance have been set to unity to match convention in NR simulations.

The spin contributions to the mode amplitudes can be

found in Refs. [52–54]. The spin contributions to the waveform modes *relative to the (2, 2) mode* up to  $\mathcal{O}(v^6)$  are:

$$\begin{aligned} \hat{A}_{21}^{(\text{PN}, \text{S})} &= -\frac{1}{2}v^2(\chi_a + \delta\chi_s) + \frac{1}{252}v^4[(-251 + 947\eta)\chi_a + 251\delta(-1 + \eta)\chi_s] \\ &\quad + \frac{1}{6}v^6(\chi_a + \delta\chi_s)(3\pi - 4\delta\chi_a + 4(-1 + \eta)\chi_s) + \mathcal{O}(v^6) \end{aligned} \quad (\text{B2a})$$

$$\hat{A}_{32}^{(\text{PN}, \text{S})} = \frac{4}{3}\sqrt{\frac{5}{7}}\left[\eta v^3\chi_s + \frac{1}{84}v^5(7\delta(31\eta - 4)\chi_a + ((81 - 208\eta)\eta - 28)\chi_s)\right] + \mathcal{O}(v^6) \quad (\text{B2b})$$

$$\hat{A}_{43}^{(\text{PN}, \text{S})} = -\frac{9}{8}\sqrt{\frac{5}{14}}v^4\eta(\chi_a - \delta\chi_s) + \mathcal{O}(v^6) \quad (\text{B2c})$$

$$\hat{A}_{41}^{(\text{PN}, \text{S})} = -\frac{1}{168}\sqrt{\frac{5}{2}}v^4\eta(\chi_a - \delta\chi_s) + \mathcal{O}(v^6) \quad (\text{B2d})$$

Note that these expressions are given relative to the (2, 2) mode, and thus differ from the expressions for individual  $(\ell, m)$  mode amplitudes typically reported in the literature.

### Appendix C: Aligned-Spin Fit Snapshots

Figs. 7–9 compare the leading-order PN-inspired fits and the quadratic fits, omitting the linear fits for simplicity. To aid in visualization, these figures are also available as interactive 3-dimensional plots in Ref. [57].

[1] S. Soni *et al.* (LIGO), Class. Quant. Grav. **42**, 085016 (2025), arXiv:2409.02831 [astro-ph.IM].

[2] J. Aasi *et al.* (LIGO Scientific), Class. Quant. Grav. **32**, 074001 (2015), arXiv:1411.4547 [gr-qc].

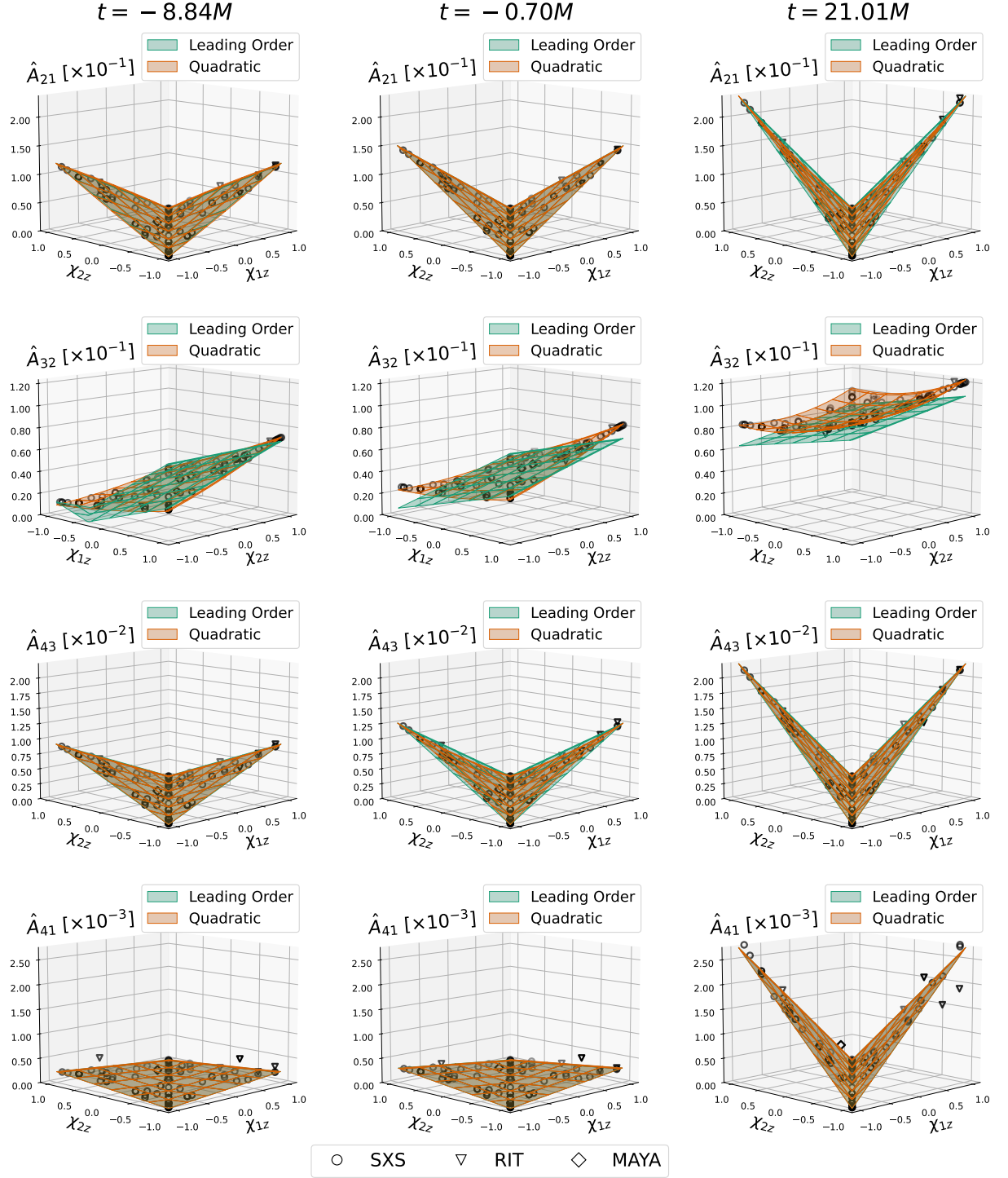


FIG. 7. *Leading-order and quadratic fit snapshots for aligned-spin simulations with  $\mathbf{q} = 1.0$ :* Snapshots of the  $(\ell, m)$ -mode amplitudes, normalized to the  $(2, 2)$  mode, at selected times  $t$  relative to the peak of the  $(2, 2)$  mode, displayed on a grid of  $\chi_{1z}$  and  $\chi_{2z}$ . Best-fit surfaces based on the leading-order fits (green) defined in Eq. 8 and the quadratic fits (orange) defined in Eq. 10 are shown. The best-fit surfaces were obtained using data from the SXS catalog only. Markers denote the NR catalog associated with each data point. All plots are oriented facing the plane defined by the leading-order dependence on  $\chi_s$  and  $\chi_a$ .



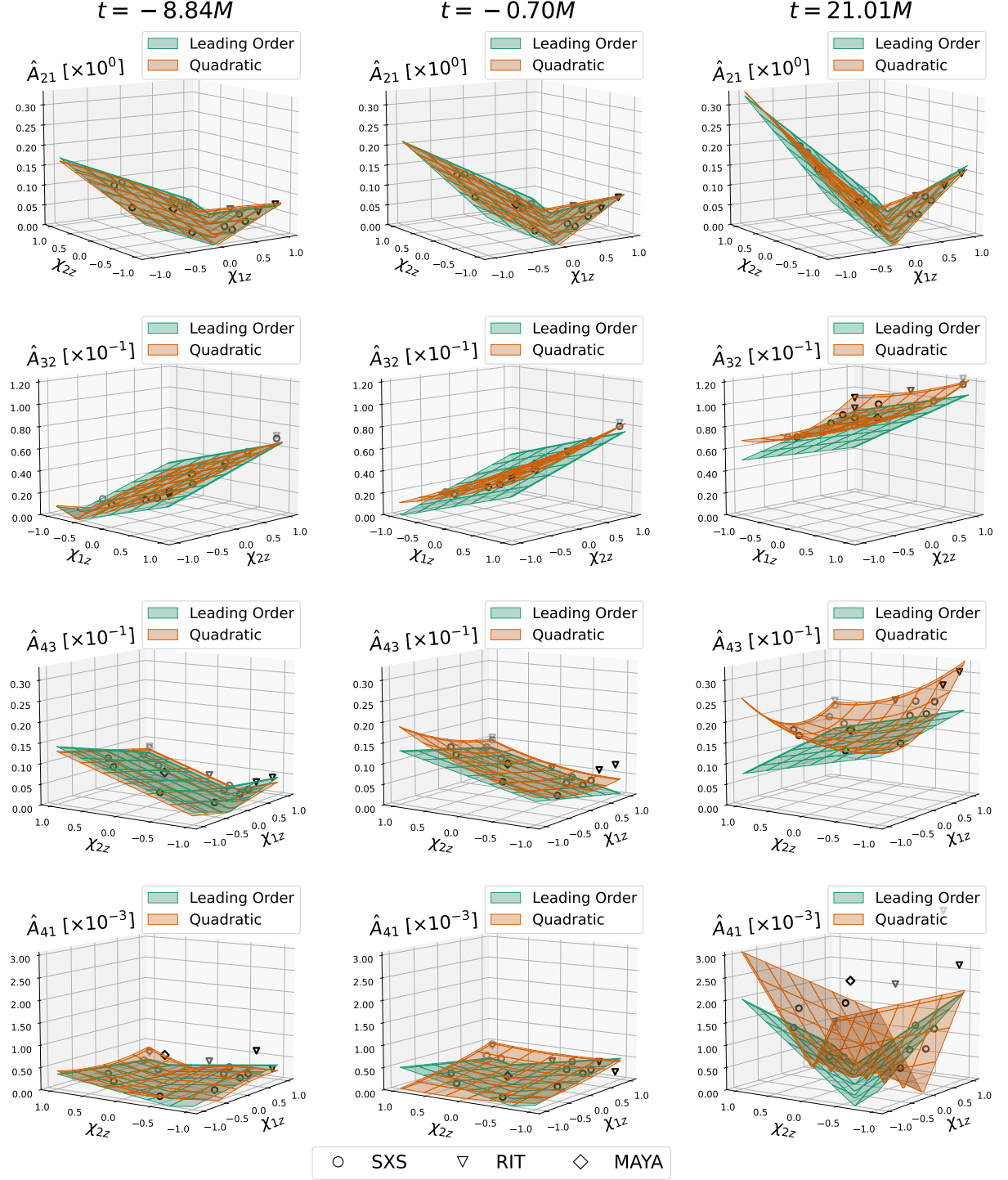


FIG. 8. *Leading-order and quadratic fit snapshots for aligned-spin simulations with  $\mathbf{q} = 1.5$ :* Snapshots of the  $(\ell, m)$ -mode amplitudes, normalized to the  $(2, 2)$  mode, at selected times  $t$  relative to the peak of the  $(2, 2)$  mode, displayed on a grid of  $\chi_{1z}$  and  $\chi_{2z}$ . Best-fit surfaces based on the leading-order fits (green) defined in Eq. 8 and the quadratic fits (orange) defined in Eq. 10 are shown. The best-fit surfaces were obtained using data from the SXS catalog only. Markers denote the NR catalog associated with each data point. All plots are oriented facing the plane defined by the leading-order dependence on  $\chi_s$  and  $\chi_a$ .

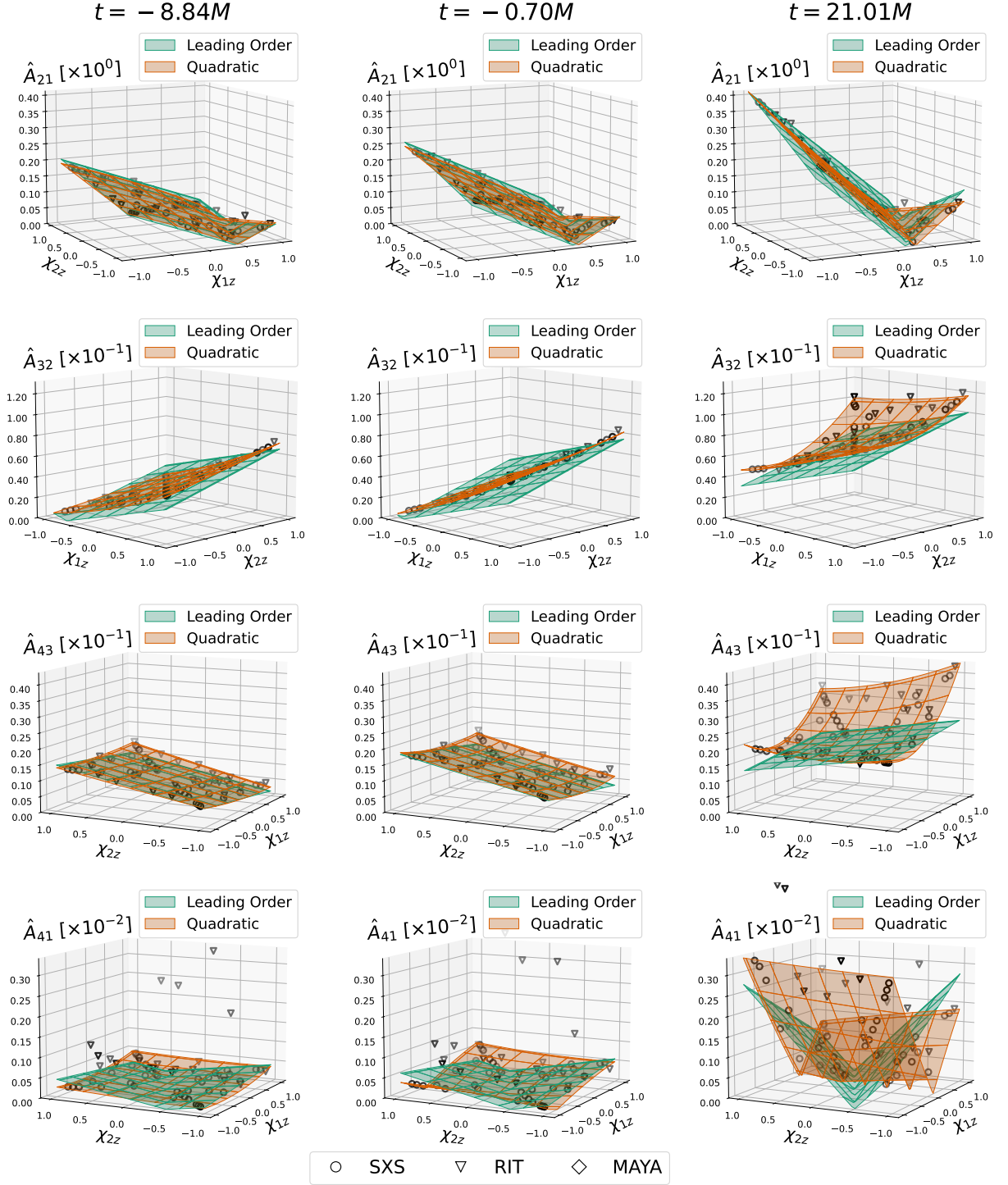


FIG. 9. *Leading-order and quadratic fit snapshots for aligned-spin simulations with  $\mathbf{q} = 2.0$ :* Snapshots of the  $(\ell, m)$ -mode amplitudes, normalized to the  $(2, 2)$  mode, at selected times  $t$  relative to the peak of the  $(2, 2)$  mode, displayed on a grid of  $\chi_{1z}$  and  $\chi_{2z}$ . Best-fit surfaces based on the leading-order fits (green) defined in Eq. 8 and the quadratic fits (orange) defined in Eq. 10 are shown. The best-fit surfaces were obtained using data from the SXS catalog only. Markers denote the NR catalog associated with each data point. All plots are oriented facing the plane defined by the leading-order dependence on  $\chi_s$  and  $\chi_a$ .

- [3] F. Acernese *et al.* (VIRGO), *Class. Quant. Grav.* **32**, 024001 (2015), arXiv:1408.3978 [gr-qc].
- [4] T. Akutsu *et al.* (KAGRA), *PTEP* **2021**, 05A101 (2021), arXiv:2005.05574 [physics.ins-det].
- [5] L. Lehner and F. Pretorius, *Ann. Rev. Astron. Astrophys.* **52**, 661 (2014), arXiv:1405.4840 [astro-ph.HE].
- [6] L. Blanchet, *Living Rev. Rel.* **17**, 2 (2014), arXiv:1310.1528 [gr-qc].
- [7] E. Berti, V. Cardoso, and A. O. Starinets, *Class. Quant. Grav.* **26**, 163001 (2009), arXiv:0905.2975 [gr-qc].
- [8] B. J. Kelly and J. G. Baker, *Phys. Rev. D* **87**, 084004 (2013), arXiv:1212.5553 [gr-qc].
- [9] R. Abbott *et al.* (LIGO Scientific, Virgo), *Phys. Rev. Lett.* **125**, 101102 (2020), arXiv:2009.01075 [gr-qc].
- [10] A. G. Abac *et al.* (LIGO Scientific, VIRGO, KAGRA), (2025), arXiv:2507.08219 [astro-ph.HE].
- [11] S. Borhanian, K. G. Arun, H. P. Pfeiffer, and B. S. Sathyaprakash, *Class. Quant. Grav.* **37**, 065006 (2020), arXiv:1901.08516 [gr-qc].
- [12] I. Kamaretsos, M. Hannam, and B. Sathyaprakash, *Phys. Rev. Lett.* **109**, 141102 (2012), arXiv:1207.0399 [gr-qc].
- [13] I. Kamaretsos, M. Hannam, S. Husa, and B. S. Sathyaprakash, *Phys. Rev. D* **85**, 024018 (2012), arXiv:1107.0854 [gr-qc].
- [14] T. Islam, (2024), arXiv:2403.03487 [gr-qc].
- [15] F. Nobili, S. Bhagwat, C. Pacilio, and D. Gerosa, *Phys. Rev. D* **112**, 044058 (2025), arXiv:2504.17021 [gr-qc].
- [16] C. Pacilio, S. Bhagwat, F. Nobili, and D. Gerosa, *Phys. Rev. D* **110**, 103037 (2024), arXiv:2408.05276 [gr-qc].
- [17] L. London, D. Shoemaker, and J. Healy, *Phys. Rev. D* **90**, 124032 (2014), [Erratum: *Phys. Rev. D* **94**, 069902 (2016)], arXiv:1404.3197 [gr-qc].
- [18] B. Bruegmann, J. A. Gonzalez, M. Hannam, S. Husa, U. Sperhake, and W. Tichy, *Phys. Rev. D* **77**, 024027 (2008), arXiv:gr-qc/0610128.
- [19] M. A. Scheel *et al.*, (2025), arXiv:2505.13378 [gr-qc].
- [20] M. Boyle *et al.*, *Class. Quant. Grav.* **36**, 195006 (2019), arXiv:1904.04831 [gr-qc].
- [21] G. Carullo, *JCAP* **10**, 061, arXiv:2406.19442 [gr-qc].
- [22] J. Healy, C. O. Lousto, and Y. Zlochower, *Phys. Rev. D* **96**, 024031 (2017), arXiv:1705.07034 [gr-qc].
- [23] J. Healy and C. O. Lousto, *Phys. Rev. D* **102**, 104018 (2020), arXiv:2007.07910 [gr-qc].
- [24] K. Jani, J. Healy, J. A. Clark, L. London, P. Laguna, and D. Shoemaker, *Class. Quant. Grav.* **33**, 204001 (2016), arXiv:1605.03204 [gr-qc].
- [25] D. Ferguson *et al.*, *Phys. Rev. D* **112**, 044043 (2025), arXiv:2309.00262 [gr-qc].
- [26] K. S. Thorne, *Rev. Mod. Phys.* **52**, 299 (1980).
- [27] L. E. Kidder, *Phys. Rev. D* **77**, 044016 (2008), arXiv:0710.0614 [gr-qc].
- [28] C. K. Mishra, A. Kela, K. G. Arun, and G. Faye, *Phys. Rev. D* **93**, 084054 (2016), arXiv:1601.05588 [gr-qc].
- [29] B. P. Abbott *et al.* (LIGO Scientific, Virgo), *Phys. Rev. Lett.* **116**, 061102 (2016), arXiv:1602.03837 [gr-qc].
- [30] S. Husa, J. A. Gonzalez, M. Hannam, B. Bruegmann, and U. Sperhake, *Class. Quant. Grav.* **25**, 105006 (2008), arXiv:0706.0740 [gr-qc].
- [31] G. Lovelace *et al.*, *Class. Quant. Grav.* **33**, 244002 (2016), arXiv:1607.05377 [gr-qc].
- [32] SpEC: Spectral Einstein Code — black-holes.org, <https://www.black-holes.org/code/SpEC.html>.
- [33] H. Friedrich, *Commun. Math. Phys.* **100**, 525 (1985).
- [34] D. Garfinkle, *Phys. Rev. D* **65**, 044029 (2002), arXiv:gr-qc/0110013.
- [35] F. Pretorius, *Class. Quant. Grav.* **22**, 425 (2005), arXiv:gr-qc/0407110.
- [36] M. Boyle, K. Mitman, M. Scheel, and L. Stein, The sxs package (2025).
- [37] SXS Collaboration, The sxs catalog of simulations v3.0.0 (2025).
- [38] Y. Zlochower, J. G. Baker, M. Campanelli, and C. O. Lousto, *Phys. Rev. D* **72**, 024021 (2005), arXiv:gr-qc/0505055.
- [39] M. Ansorg, B. Bruegmann, and W. Tichy, *Phys. Rev. D* **70**, 064011 (2004), arXiv:gr-qc/0404056.
- [40] J. Healy, C. O. Lousto, H. Nakano, and Y. Zlochower, *Class. Quant. Grav.* **34**, 145011 (2017), [Erratum: *Class. Quant. Grav.* **40**, 249502 (2023)], arXiv:1702.00872 [gr-qc].
- [41] T. W. Baumgarte and S. L. Shapiro, *Phys. Rev. D* **59**, 024007 (1998), arXiv:gr-qc/9810065.
- [42] M. Shibata and T. Nakamura, *Phys. Rev. D* **52**, 5428 (1995).
- [43] T. Nakamura, K. Oohara, and Y. Kojima, *Prog. Theor. Phys. Suppl.* **90**, 1 (1987).
- [44] T. Goodale, G. Allen, G. Lanfermann, J. Massó, T. Radke, E. Seidel, and J. Shalf, in *Vector and Parallel Processing – VECPAR’2002, 5th International Conference, Lecture Notes in Computer Science* (Springer, Berlin, 2003).
- [45] F. Löffler *et al.*, *Class. Quant. Grav.* **29**, 115001 (2012), arXiv:1111.3344 [gr-qc].
- [46] E. Schnetter, S. H. Hawley, and I. Hawke, *Class. Quant. Grav.* **21**, 1465 (2004), arXiv:gr-qc/0310042.
- [47] Center for Computational Relativity and Gravitation (CCRG)@RIT, Catalog of numerical simulations, <https://ccrg.rit.edu/numerical-simulations> (n.d.), accessed: 2025-07-17.
- [48] Center for Gravitational Physics Storage @ UT Austin, Waveforms, <https://cgpstorage.ph.utexas.edu/waveforms/> (n.d.), accessed: 2025-07-17.
- [49] D. Ferguson, S. Anne, M. Gracia-Linares, H. Iglesias, A. Jan, E. Martinez, L. Lu, F. Meoni, R. Nowicki, M. Trostel, B.-J. Tsao, and F. Valorz, *mayawaves* (2023).
- [50] C. J. Woodford, M. Boyle, and H. P. Pfeiffer, *Phys. Rev. D* **100**, 124010 (2019), arXiv:1904.04842 [gr-qc].
- [51] M. A. Shaikh, V. Varma, A. Ramos-Buades, H. P. Pfeiffer, M. Boyle, L. E. Kidder, and M. A. Scheel, (2025), arXiv:2507.08345 [gr-qc].
- [52] K. G. Arun, A. Buonanno, G. Faye, and E. Ochsner, *Phys. Rev. D* **79**, 104023 (2009), [Erratum: *Phys. Rev. D* **84**, 049901 (2011)], arXiv:0810.5336 [gr-qc].
- [53] Q. Henry, S. Marsat, and M. Khalil, *Phys. Rev. D* **106**, 124018 (2022), arXiv:2209.00374 [gr-qc].
- [54] Y. Pan, A. Buonanno, A. Taracchini, L. E. Kidder, A. H. Mroué, H. P. Pfeiffer, M. A. Scheel, and B. Szilágyi, *Phys. Rev. D* **89**, 084006 (2014), arXiv:1307.6232 [gr-qc].
- [55] C. Mills and S. Fairhurst, *Phys. Rev. D* **103**, 024042 (2021), arXiv:2007.04313 [gr-qc].
- [56] P. Virtanen *et al.*, *Nature Meth.* **17**, 261 (2020), arXiv:1907.10121 [cs.MS].
- [57] V. A. Cáceres-Barbosa, Interactive plots for GW mode amplitude fits (2025), accessed: 2025-07-20.